PAPER

Check for updates

A Grignard-mediated route to access 4-substituted-3-*E*-styryl-2*H*-chromenes: alternate extrinsic FRET probes to explore the IIA and IIIA subdomains of serum proteins

Soumyadipta Rakshit,*[a] Sanjay Bhar[b] and Rimi Roy [ID] *[c]

A facile and efficient strategy to construct 2*H*-chromene scaffolds, employing variably substituted spiro-4-oxochroman-3,1′-cyclopropane precursors under mild conditions, is proposed in this study. The transformation proceeds *via* a ring-opening reaction of cyclopropane mediated by Grignard reagents and furnishes a series of C-3 functionalized 2*H*-chromenes in good to excellent yields (88–96%) with a broad degree of functional group tolerance. The potential of these diversified 2*H*-chromenes as effective fluorescence probes is demonstrated using steady-state, time-resolved emission measurements. In-depth investigations of the interactions of this new class of molecular scaffolds with model proteins through structure-optical signalling relationship studies led to the development of them as new extrinsic fluorescence resonance energy transfer (FRET) probes that are able quantify the IIA binding site of human serum albumin (HSA) and the IIIA binding site of bovine serum albumin (BSA). Steady-state and time-resolved fluorescence data appended with circular dichroism (CD) studies reveal swift inclusion without altering the conformation of the secondary structure of the protein. Molecular docking calculations confirm the hydrophobic cavities of subdomain IIA of HSA and IIIA of BSA to be the binding sites of 2*H*-chromenes. The calculated average distance between the protein donor and 2*H*-chromenes was found to be in good agreement with the experimental outcomes.

1. Introduction

Over the years, cyclopropanes have emerged as imperative synthons in many organic transformations due to their unique reactivity associated with the highly strained three-membered carbocycle. Ring-opening reactions of suitably substituted cyclopropane motifs are synthetic approaches to a plethora of complex heterocycles. 2*H*-Chromenes and their derivatives are ubiquitous oxygenated heterocycles that are present in a myriad of biologically relevant molecules and key pharmaceuticals.[1–3] They serve as expedient therapeutic agents and drug candidates with anti-HIV, anticancer, antitumor, antitubercular, anti-inflammatory, antibacterial/antimicrobial, antidiabetic, fungicidal, and antioxidant activities.[4,5] Moreover, 2*H*-chromenes have been applied extensively in optical brighteners, organic light-emitting diodes (OLEDs), non-linear optical chromophores, organic scintillators, chemical sensors, and dye lasers owing to their remarkable photophysical properties.[6,7] Besides

their minimal toxicity, these molecular skeletons are often exploited as promising intermediates in the synthesis of sophisticated polycyclic frameworks and complex bioactive natural products.[8] Interest in the chemistry of chromenes continues unabated, majorly due to their multifarious applications in pharmacological and biological fields, which have made them one of the most privileged scaffolds to work on; to date, considerable synthetic routes have been developed to access 2*H*-chromene architectures. Among these, one of the attractive pathways to construct these core structures comprises the use of metal-mediated methodologies, such as ring-closing olefin metathesis,[9] cyclization of aryl propargyl ethers[10] and domino C–H activation reactions.[11,12] Other notable approaches include the metal-free Brønsted and Lewis acid/base-catalyzed inter- and intra-molecular annulations of phenol or salicylaldehyde equivalents.[13,14] Despite their merits, many of the reported techniques employ exotic and prefunctionalized metal catalysts, often in high loading; they require elevated reaction temperatures, multistep procedures, involves complex product isolation methods, and suffer from a narrow substrate scope and relatively low product yields. Hence, the development of a facile and economically viable route toward achieving structurally diverse 2*H*-chromenes from readily available substrates with decent tolerance for various functional groups is

[a]Department of Chemistry, Motilal Nehru National Institute of Technology Allahabad, Prayagraj – 211004, Uttar Pradesh, India. E-mail: srakshit@mnnit.ac.in

[b]Department of Chemistry, Jadavpur University, 188, Raja S.C. Mallick Road, Kolkata – 700032, West Bengal, India

[c]Department of Chemistry, Presidency University (Main Campus), 86/1, College Street, Kolkata – 700073, West Bengal, India. E-mail: rimi.chem@presiuniv.ac.in

a challenging yet necessary goal. Given the aforementioned objectives and following our continuous interest in the ring-opening reactions of cyclopropyl motifs, herein, we have established an efficient method for the straightforward access to C-3 functionalized 2H-chromenes from differently substituted spiro-4-oxochroman-3,1′-cyclopropanes utilizing the Grignard reaction. Organomagnesium compounds are among the low-priced and most used organometallic reagents in organic synthesis. Owing to their higher reactivity, widespread availability, enhanced tunability and improved atom efficiency as they transfer entire nucleophilic functionality to the substrate, Grignard reagents offer a fundamental platform to make multifunctionalized molecules in a single step without involving a harsh reaction environment; thereby, they facilitate the survival of a variety of sensitive substituents through a selective process. It is noteworthy that the present work using the Grignard addition constitutes an operationally simple synthetic strategy to generate 2H-chromene frameworks under exceedingly mild conditions without the need for additional catalysts or activating agents, tolerates a wide range of functional groups, and delivers an unprecedented array of 4-alkyl/allyl/phenyl-3-E-styryl-2H-chromenes in excellent yields.

Literature surveys have disclosed that the majority of the related articles are dedicated to the synthesis of 2H-chromenes, while investigations on their protein binding affinity are scarce. We considered serum albumin proteins as suitable models for understanding molecular recognition in protein–ligand interactions. Serum albumins are responsible for innumerable physiological functions, like the transportation and disposition of fatty acids, amino acids, metalloenzymes, proteins, etc., and also affect the distribution of metabolites.[15,16] Because of their wide abundance in blood plasma,[17–19] together with their extraordinary ligand binding properties, serum albumins are considered to be the perfect candidates to envisage the protein–ligand[20–24] and protein–solvent interactions.[25] With albumin being the major drug carrier in the body, ligands binding with albumins basically influence the pharmacological impact of the drugs; thus, monitoring the drug–albumin interaction is indispensable in determining the bioavailability, pharmacokinetics and pharmacodynamics.[20,21,26] Because of its structural homology (∼76%) with HSA, bovine serum albumin (BSA) has been studied extensively and is also often used as a model system for human in vivo interactions.[27] Thus, a thorough understanding of the interactions between potential bioactive 2H-chromene cores with serum albumins (HSA and BSA in this case) is of great importance for a better perception of the protein structure–function and drug design.[28] Crystallographic

analysis revealed that HSA and BSA contain 585 and 582 amino acid residues and are composed of mainly three homologous domains, namely I, II, III which are further divided into two subdomains A and B. BSA contains two tryptophan (Trp) residues (Trp-134 present in the subdomain IA and Trp-212 in the subdomain IIA), whereas HSA has only one (Trp-214 residing in the subdomain IIA).[29,30] Upon interaction with ligand or drug or nucleic acid or lipid molecules, etc., the intrinsic fluorescence of the Trp residues is altered.[31]

The binding proficiency of the prepared 2H-chromenes with the most frequently studied serum albumins (HSA and BSA) was further explored under physiological conditions. In this aspect, we opted for a non-invasive fluorescence technique by monitoring the tryptophan fluorescence of both serum albumins. The changes brought about by 2H-chromenes on proteins were systematically analyzed by steady-state and time-resolved fluorescence spectroscopy, circular dichroism (CD) spectroscopy, and molecular docking to unveil the mechanisms underlying the interaction, micropolarity of the environment and fluorescence resonance energy transfer (FRET). We hope that this elaborate study will pave the way not only for the design of more 2H-chromene variants as effective fluorescent probes for the spectroscopic investigation of a model biological system, but will also provide insight into the molecular basis of the interactions between them.

2. Results and discussion

2.1. Synthesis of the 4-substituted-3-E-styryl-2H-chromenes

At the outset, 6-methyl-4-chromanone and 4-chromanone were condensed with substituted aryl aldehydes in alcoholic HCl[32] under reflux to afford the corresponding E-3-arylidene-chroman-4-ones in good yields.[33] Cyclopropanation of these chromanochalcones with dimethylsulfoxonium methylide, generated in situ by $^{n}Bu_4N^{+}Br^{-}$-mediated deprotonation of trimethylsulfoxonium iodide under basic conditions,[34] furnished the spiro-4-oxochroman-3,1′-cyclopropanes **1**, which were employed as substrates for the Grignard addition reaction. To commence our investigation, spiro-4-oxochroman-3,1′-cyclopropane **1a** and MeMgI were chosen as the initial model, in anhydrous ether (Scheme 1). Since strongly coordinating Mg^{2+} ions in the reaction mixture inhibited dehydration, an intermediate acidic workup with aq. NH$_4$Cl was subsequently performed. To our delight, the reaction with MeMgI led to the cleavage of the cyclopropyl ring in **1a** after the workup and afforded the diene, 3-(4-methoxystyryl)-4,6-dimethyl-2H-chromene **2a** in 91% yield (entry 1, Table 1).
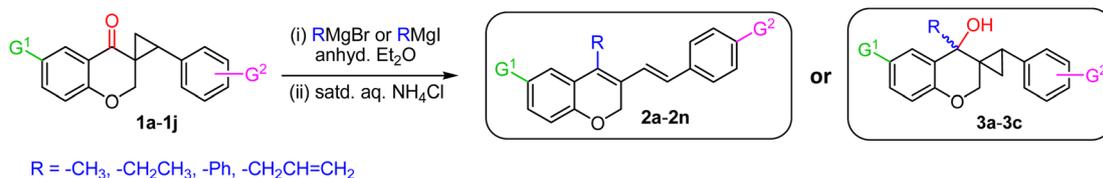
Scheme 1 Synthesis of 4-alkyl/allyl/phenyl-3-E-styryl-2H-chromenes using different Grignard reagents.

Table 1 Reaction of spiro-4-oxochroman-3,1′-cyclopropanes with Grignard reagents
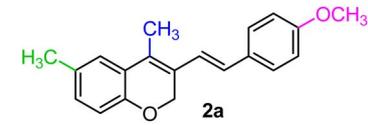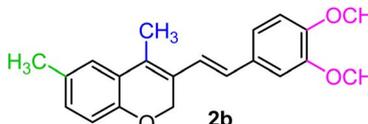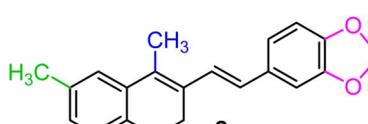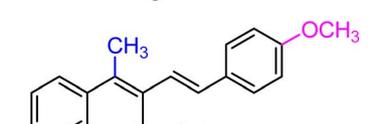
Entry	G^1, G^2, R	Substrate (1)	Product (2/3)	Time (h)/yield[a] (%)
1	CH_3, 4-OCH_3, CH_3	1a	2a	5/91
2	CH_3, 3,4-$(OCH_3)_2$, CH_3	1b	2b	5/88
3	CH_3, 3,4-OCH_2O-, CH_3	1c	2c	5/89
4	H, 4-OCH_3, CH_3	1d	2d	4/96
5	H, 3,4-$(OCH_3)_2$, CH_3	1e	2e	4/94
6	H, 3,4-OCH_2O-, CH_3	1f	2f	4/92
7	H, 2-thiophene, CH_3	1g	2g	4/90
8	H, 4-OCH_3, Et	1d	2h	6/90
9	H, 3,4-OCH_2O-, Et	1f	2i	6/92
10	H, 4-OCH_3, Ph	1d	2j	6/91
11	H, 3,4-$(OCH_3)_2$, Ph	1e	2k	6/89
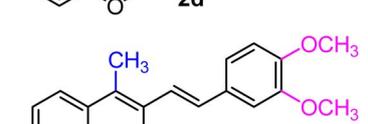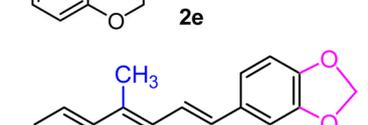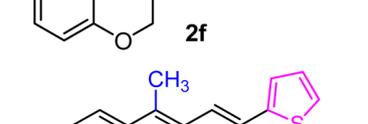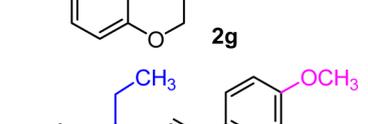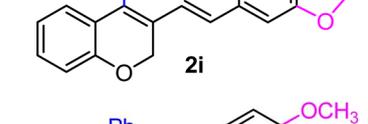
Paper
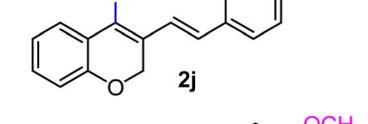
Table 1 (*Contd.*)

Entry	G^1, G^2, R	Substrate (**1**)	Product (**2/3**)	Time (h)/yield[a] (%)
12	H, 3,4-OCH$_2$O–, Ph	**1f**	**2l**	6/90
13	H, 4-OCH$_3$, allyl	**1d**	**2m**	6/89
14	H, 3,4-OCH$_2$O–, allyl	**1f**	**2n**	6/91
15	CH$_3$, 2-OCH$_3$, CH$_3$	**1h**	**3a**	5/93[b]
16	H, 3-OCH$_3$, CH$_3$	**1i**	**3b**	5/94[c]
17	H, 4-Cl, CH$_3$	**1j**	**3c**	5/95[c]
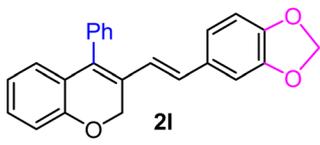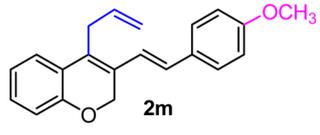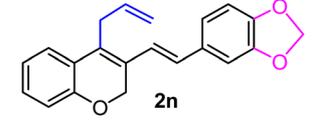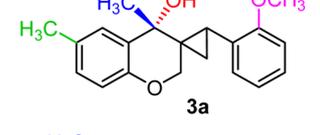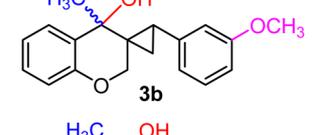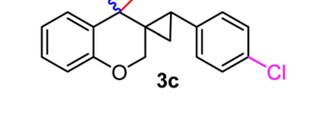
[a] Isolated yield of the pure product characterized spectroscopically. [b] 1 : 13 mixture of diene and cyclopropyl carbinol **3a** was obtained, out of which the alcohol **3a** was isolated by crystallization. [c] Cyclopropyl alcohols **3b** and **3c** were acquired as an inseparable 1 : 1 diastereomeric mixture.

Analysis of the ^{1}H NMR spectrum of **2a** revealed the absence of the triplet signal at δ 2.95 (t, J = 8.5 Hz, 1H) and double doublets at δ 2.00 (dd, J_1 = 8.9 Hz, J_2 = 4.7 Hz, 1H) and δ 1.32 (dd, J_1 = 7.2 Hz, J_2 = 4.8 Hz, 1H), assigned to the cyclopropyl moiety, further confirming the disappearance of the cyclopropane core under the applied reaction conditions. In addition, two distinct doublets arose at δ 7.14 (d, J = 16.4 Hz, 1H) and δ 6.45 (d, J = 16.4 Hz, 1H), respectively, which clearly demonstrated the generation of an olefinic bond with a *trans*-configuration. Encouraged by the preliminary result, we assessed the generality of this process by allowing a variety of substituted spiro-4-oxochroman-3,1′-cyclopropanes (**1a–1j**) to react in the presence of methyl, ethyl, allyl, and phenyl Grignard reagents (3.0 equiv.). The above reactions proceeded smoothly in anhydrous ether and were accomplished within 4–6 hours under an inert atmosphere. The results are summarized in Table 1.

As per the data given in Table 1, spiro-4-oxochroman-3,1′-cyclopropanes (**1a–1g**) with an electron-releasing group at the *para*-position of the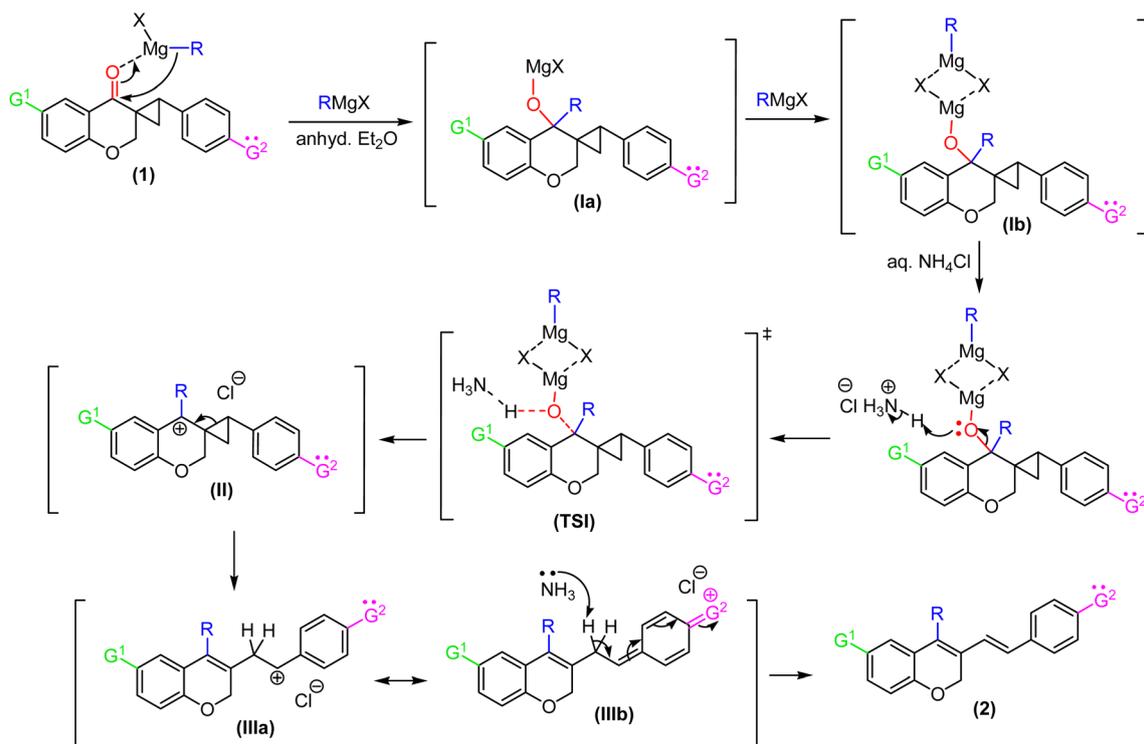 aromatic ring attached to the cyclopropyl moiety produced 4-alkyl/allyl/phenyl-3-*E*-styryl-2*H*-chromenes (**2a–2n**) exclusively in high yields (88–96%, entries 1–14) upon treatment with different Grignard reagents followed by dehydration. Structural assignments for the synthesized adducts **2** were achieved by means of ^{1}H NMR, ^{13}C NMR, and HRMS analyses (Fig. S21–S71). All the products **2** were found to entail an exocyclic olefin linkage with *E*-configuration, unambiguously determined by the ^3J values (16.1–16.5 Hz) between the alkene protons. To the best of our knowledge, all these compounds **2** have borne no literature precedence to date. In this regard, the reaction of spiro-4-oxochroman-3,1′-cyclopropane **1h** substituted with an electron-donating –OMe group at the *ortho*-position of the phenyl ring at the carbinyl carbon, turned out to be particularly interesting as it delivered a mixture of the expected diene **2o** along with a tertiary cyclopropyl alcohol **3a** in a 1 : 13 ratio, under identical conditions (entry 15). Although the alcohol was successfully isolated using fractional crystallization, the diene **2o** could not be purified from the mother liquor despite several attempts. The location of the substituents on the benzene nucleus linked to the cyclopropyl core had a marked effect on the outcome of the transformation. As for the substrate

Scheme 2 Proposed mechanism for the Grignard reagent-mediated ring-opening process.

1i, where an electron-releasing group (OMe) was at the *meta*-position of the aromatic ring connected to the cyclopropane, the corresponding cyclopropyl carbinol **3b** was acquired solely as an inseparable 1:1 diastereomeric mixture (yield 94%, entry 16). Notably, when the aromatic ring at the cyclopropyl carbon bore an electron-withdrawing Cl substituent **1j,** three-membered ring scission was completely suppressed, and the exclusive product was identified to be a mixture of 1:1 diastereomeric cyclopropyl alcohol **3c** (yield 95%, entry 17). Altogether, the results depicted in Table 1 indicate that the electronic nature as well as the position of the substituents on the aryl part play a crucial role in determining the reactivity of the spiro-4-oxo-chroman-3,1′-cyclopropanes **1** toward the Grignard reagent. The present protocol has been proven effective in terms of compatibility with various functional groups, including alkyl, phenyl, halide, methylenedioxy and allyl, which survived throughout the said process. Remarkably, in the case of the allyl group (entries 13 and 14 in Table 1), isomerization of the terminal double bond did not take place under the applied conditions, despite having the opportunity to attain greater stability owing to extended conjugation. This was quite evident in the ^{1}H NMR of **2m,** where a 2*H* multiplet appeared at δ 3.52–3.50, corresponding to the methylene protons. Of late, the strict demand of pharmaceutical industries to acquire products free of any transition-metal impurities has prioritized the use of transition-metal-free protocols in synthesis.[8] In that regard, our present synthetic methodology, which excludes the usage of any transition metal catalyst, appears particularly attractive to furnish differently substituted 2*H*-chromenes with significant functional attributes and high yield.

A plausible mechanistic pathway for the Grignard-mediated ring-opening process is delineated in Scheme 2. The reaction likely begins with coordination of the Grignard reagent to the carbonyl centre of **1,** followed by nucleophilic attack to generate the magnesium alkoxide intermediate **Ia.** Subsequent interaction with a second equivalent of RMgX affords the dimeric complex **Ib.**[35] Upon aqueous quenching with NH$_4$Cl, protonation of the alkoxide promotes cleavage of the adjacent C–O bond, leading to formation of a benzylic tertiary carbocation **II.** This intermediate is stabilized through the inductive (+I) effect and hyperconjugation contributed by the newly introduced R group (alkyl, phenyl, or allyl substituents). The carbocation then undergoes strain-relieving cyclopropane ring scission to yield intermediate **IIIa,** which is further stabilized by conjugation with the aryl moiety. In substrates carrying *para*-substituents (G^2) with electron-donating resonance effects, an additional stabilization pathway *via* delocalization is operative (**IIIb**). Finally, facile deprotonation of the acidic methylene in **III** by ammonia affords the conjugated 2*H*-chromene **2** as the final product.

2.2. Solvatochromic study

The intriguing photophysical properties of 2*H*-chromenes continue to garner immense attention and have thus been the subject of intense investigations owing to their diverse applicability. Chromenes are efficient fluorophores with good fluorescence quantum yields.[36] Therefore, to explore the optical behavior of the synthesized 2*H*-chromenes (**2a, 2b, 2d, 2e, 2f, 2h, 2i, 2k, 2l, 2m** and **2n**) bearing various substituents, UV-vis absorption, steady state and time-resolved fluorescence
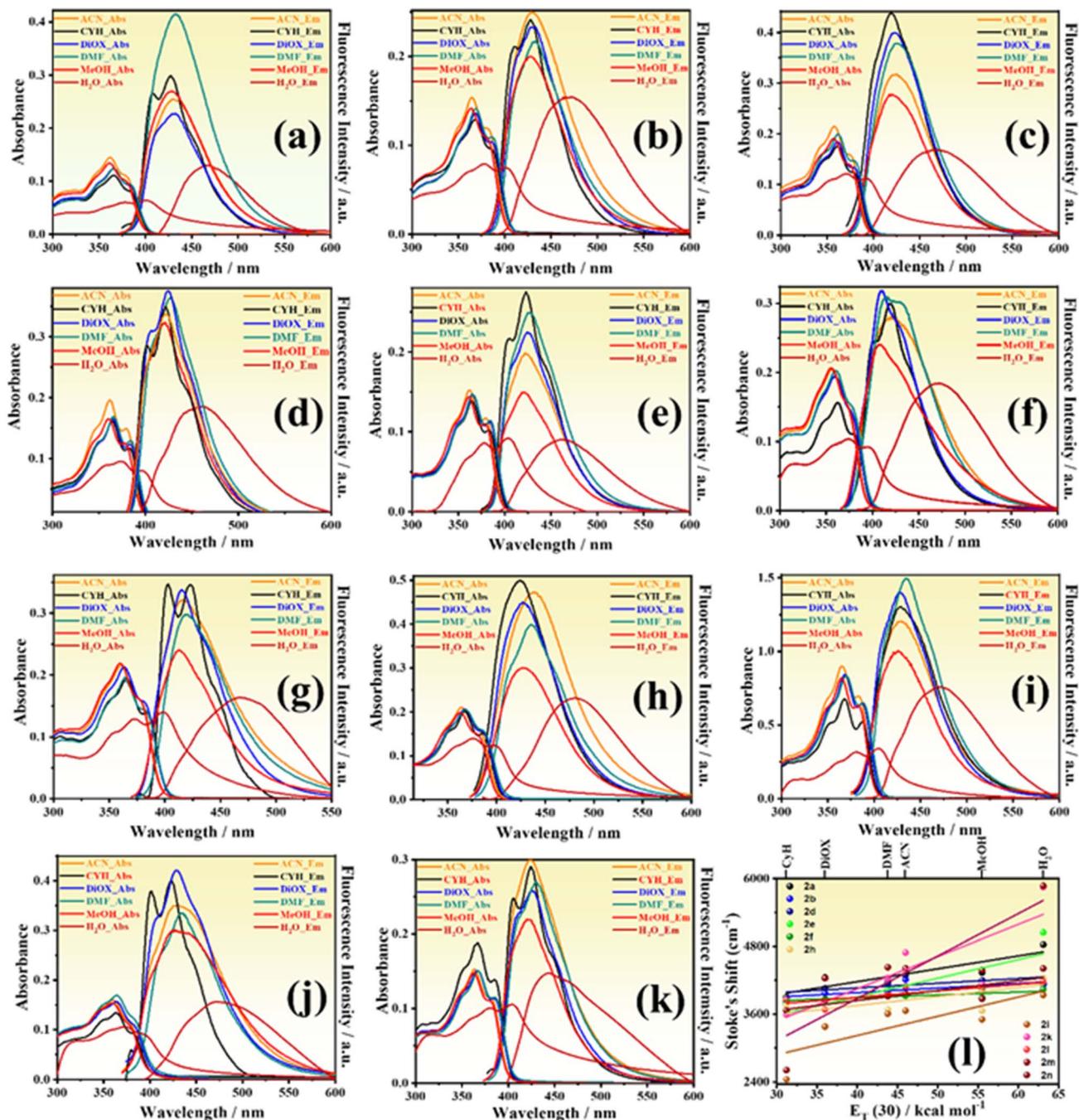
Fig. 1 Absorption and emission spectra of selected 2H-chromenes in different solvents: (a) 2a, (b) 2b, (c) 2d, (d) 2e, (e) 2f, (f) 2h, (g) 2i, (h) 2k, (i) 2l, (j) 2m and (k) 2n. The emission spectra were observed upon exciting at their corresponding absorption maxima. (l) Correlation of the solvent-induced Stokes' shift of 2H-chromenes with the $E_T(30)$ parameter.

measurements were recorded at room temperature in solvents of different polarities at a concentration of 1×10^{-6} M. The absorption and fluorescence spectra of the selected 2H-chromenes in six representative solvents, namely, acetonitrile, cyclohexane, dioxane, dimethylformamide, methanol and water, are illustrated in Fig. 1.

It is well known that the spectral behavior of an organic molecule is closely interrelated with its electronic structure in both the ground and excited states. Therefore, it is imperative to

understand the effects of different solvents on absorption and fluorescence spectra, to design novel skeletons with optical properties, to gain insight about the excited-states of fluorescent molecules, and to realize the course of the photochemical transformation.[37] Details of the absorption (λ_{abs}^{max}) and emission (λ_{em}^{max}) maxima, and quantum yields of 2H-chromenes in different solvents are listed in Table 2. The characteristic absorption maxima of 2 are seen to appear in the range from 355 to 405 nm and can be attributed to $\pi-\pi^*$ transitions.[38]

Table 2 Details of the absorption (λ_{abs}^{max}) and emission (λ_{em}^{max}) maxima and quantum yields of 2H-chromenes in different solvents

Solvent		Compound										
		2a	2b	2d	2e	2f	2h	2i	2k	2l	2m	2n
CYH	λ_{abs}^{max} (nm)	366	368	361	364	364	362	366	368	368	363	367
	λ_{em}^{max} (nm)	427	428	419	422	423	419	402	424	429	401	424
	Φ	0.19	0.23	0.22	0.19	0.23	0.19	0.20	0.27	0.22	0.21	0.15
DMF	λ_{abs}^{max} (nm)	366	369	362	365	366	360	364	368	370	364	368
	λ_{em}^{max} (nm)	432	433	426	428	428	415	419	436	434	434	430
	Φ	0.25	0.24	0.23	0.19	0.16	0.11	0.11	0.24	0.21	0.11	0.12
ACN	λ_{abs}^{max} (nm)	362	364	358	362	362	355	361	364	365	360	363
	λ_{em}^{max} (nm)	430	430	423	422	422	420	416	439	429	428	424
	Φ	0.16	0.21	0.15	0.21	0.09	0.26	0.13	0.21	0.21	0.17	0.20
DiOX	λ_{abs}^{max} (nm)	365	368	361	365	365	360	364	367	369	363	366
	λ_{em}^{max} (nm)	432	431	423	424	425	410	415	427	427	429	426
	Φ	0.20	0.20	0.22	0.20	0.17	0.23	0.20	0.25	0.23	0.18	0.11
MeOH	λ_{abs}^{max} (nm)	361	364	357	360	361	355	360	363	364	359	362
	λ_{em}^{max} (nm)	428	427	420	421	420	408	412	427	426	426	421
	Φ	0.16	0.17	0.23	0.16	0.18	0.14	0.12	0.20	0.15	0.17	0.18
H$_2$O	λ_{abs}^{max} (nm)	379	401	392	374	403	394	398	376	405	372	404
	λ_{em}^{max} (nm)	464	469	468	461	463	473	472	482	473	476	445
	Φ	0.09	0.10	0.09	0.05	0.04	0.04	0.05	0.10	0.04	0.03	0.06

The nature of the excited state and solvent polarity effects on fluorescence were investigated through a linear correlation analysis of the Stokes' shift ($\nu_a-\nu_f$) against the solvent polarity parameter $E_T(30)$ (Fig. 1l).[36,39,40] The resulting plot showed linearity with a good correlation coefficient. The slope values indicate that compounds 2i, 2k, and 2m displayed the highest sensitivity to solvent polarity, which confirms the presence of specific dipole–dipole interactions or intermolecular solute–solvent interactions.[39,41] By contrast, the other 2H-chromene analogues exhibited attenuated solvent-dependent interactions with the fluorophore.

Likewise, the fluorescence analysis disclosed a similar pattern, where compounds 2 showed emission between 401 and 482 nm. The effect of solvent polarity on the bathochromic shifts in the absorption and fluorescence spectral bands is negligible, confirming no significant change in the excited-state charge distribution or excited-state dipole moment across different solvents.[42] In apolar aprotic solvents, the fluorescence quantum yields (Φ) of the compounds were found to range from 0.15 to 0.27 (Table 2). Conversely, a considerable bathochromic shift along with peak broadening of fluorescence in aqueous media can be explained in terms of the orientation of solvent dipoles around the fluorophores to attain an energetically favourable arrangement, indicating a stronger interaction with polar protic solvents in the excited-state.[43,44] The low quantum yield in aqueous solution may be attributed to the occurrence of non-radiative pathways between the charge transfer emissive state and the ground state.[45,46]

The fluorescence lifetime decays of compounds 2 were assayed by monitoring the emission at their relevant steady-state emission maxima, and all the decays were observed to be bi-exponential, irrespective of the solvent polarity (Fig. 2). Each compound exhibited a very short component (τ_1) and a significantly longer one (τ_2). The bi-exponential decays of

compounds 2 in different solvents are likely due to two distinct local environments arising from solvent reorganization and collisional deactivation with the solvent.[37,47] The position of the compound within the solvent cluster gives rise to the short component of the fluorescence lifetime, while the long lifetime component is associated with the presence of free molecules. The particulars of the time-resolved data are provided in Table S1.

2.3. FRET with HSA and BSA

Fluorescence spectroscopy has been proven to be the most promising, efficient and sensitive non-invasive technique to elucidate various aspects of protein biophysics, such as protein folding, protein–protein interactions, and protein dynamics.[48,49] Förster resonance energy transfer (FRET) is perhaps the best-known optical probe method to utilize the optical signature as a marker for imaging and tracking the biomolecular conformational changes of protein and DNA via radiationless transitions.[50–52] According to Förster, the excitation spectrum of the acceptor must overlap with the emission spectrum of the donor.[53] Although FRET can be applied for detection at a single molecular level, its efficacy depends strongly on the distance of separation between the donor and the acceptor molecules. Thus, new extrinsic probes are designed to serve as reporters of the proteinous microenvironment.[54–56] To date, many groups have used extrinsic fluorescent probes to study the polarity of protein cavities, secondary structures and dynamics of proteins.[49,57–59]

Changes in the intrinsic fluorescence of Trp due to the modulation of the local microenvironment are considered an indication of conformational events and ligand binding properties of proteins.[49] The fluorescence spectra of HSA and BSA at physiological pH 7.4 in the presence of different 2H-chromenes are portrayed in Fig. 3 and 4 (Panel A), showing that the
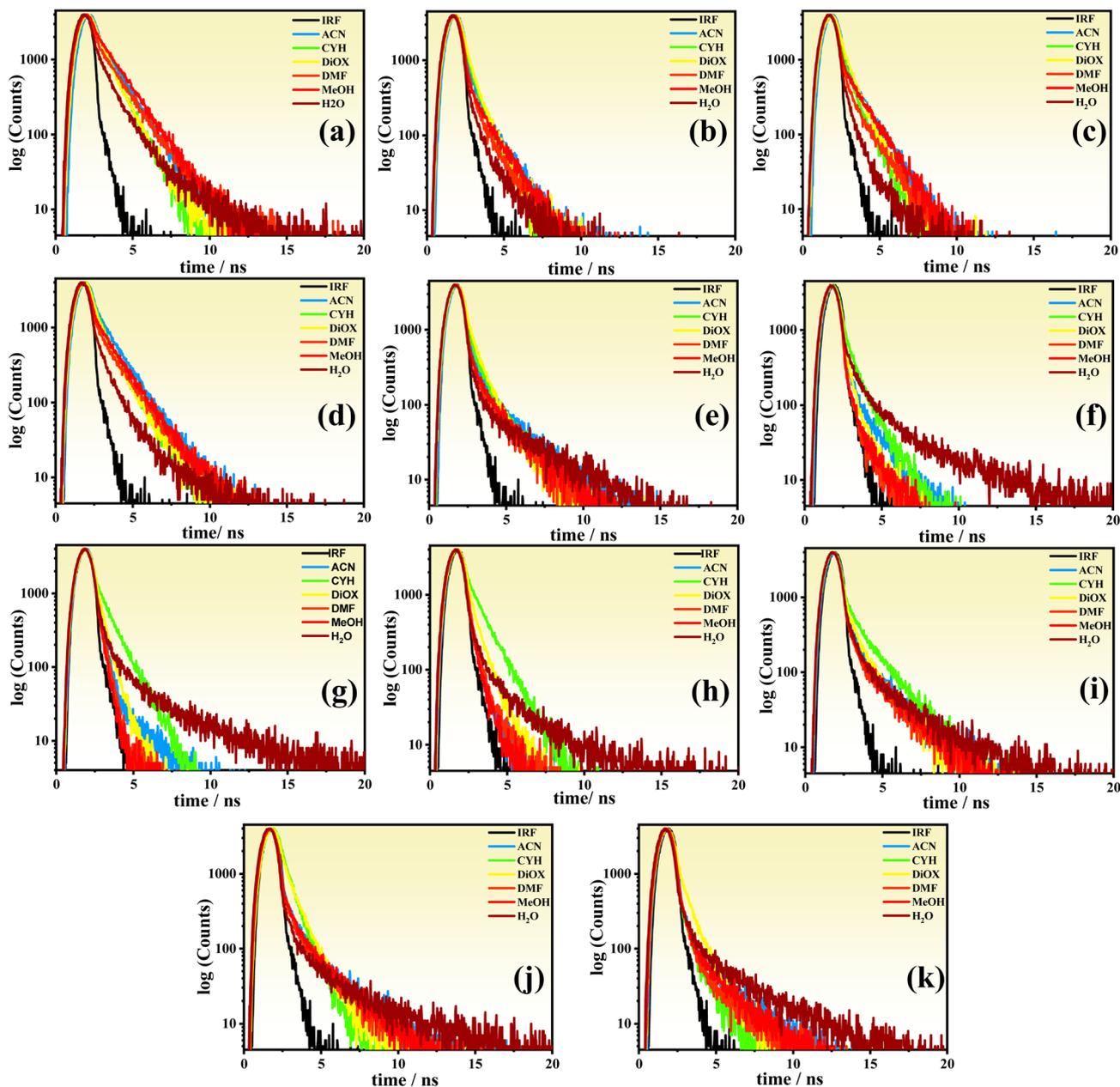
Fig. 2 Fluorescence decay curves of selected $2H$-chromenes in different solvents: (a) **2a**, (b) **2b**, (c) **2d**, (d) **2e**, (e) **2f**, (f) **2h**, (g) **2i**, (h) **2k**, (i) **2l**, (j) **2m** and (k) **2n**, monitored at their respective emission intensity maxima upon excitation at 371 nm.

successive addition of each of $2H$-chromenes results in the quenching of the fluorescence intensities of both HSA and BSA. The quenching is accompanied by the concomitant formation of a second emission band around the emission maxima, along with the formation of an iso-emissive point of each of the compounds. The emission maximum of the Trp residue of HSA and BSA undergo slight hypsochromic shifts ($\lambda_{em}^{max} \sim 325$ nm in comparison to $\lambda_{em}^{max} \sim 333$ nm of free HSA, and $\lambda_{em}^{max} \sim 335$ nm in contrast to $\lambda_{em}^{max} \sim 340$ nm of free BSA). This observation can be rationalized based on the idea of some modification of the local environments of the Trp residue imparted by the presence of the probe.[60,61]

Since the chromenes are neutral and hydrophobic in nature, it is likely to assume that the emitting Trp residue enjoys more hydrophobic surroundings in the presence of the external probe, leading to a slight blue shift in the emission maxima.[62] The linearity of the quenching plots clearly implies that a single type of quenching is taking place in the systems (Fig. S72 and S73).[49] The quenching rate constants (k_q) are of the order of 10^{13} L mol^{-1} s^{-1} (Table 3), which is quite higher than the maximum diffusion collision rate constants of various quenchers with biopolymers (in the order of 10^{10} L mol^{-1} s^{-1}).[61,63] In the case of HSA, compounds **2a, 2h, 2k, 2l**, and **2n** exhibited higher quenching compared to the others. However,

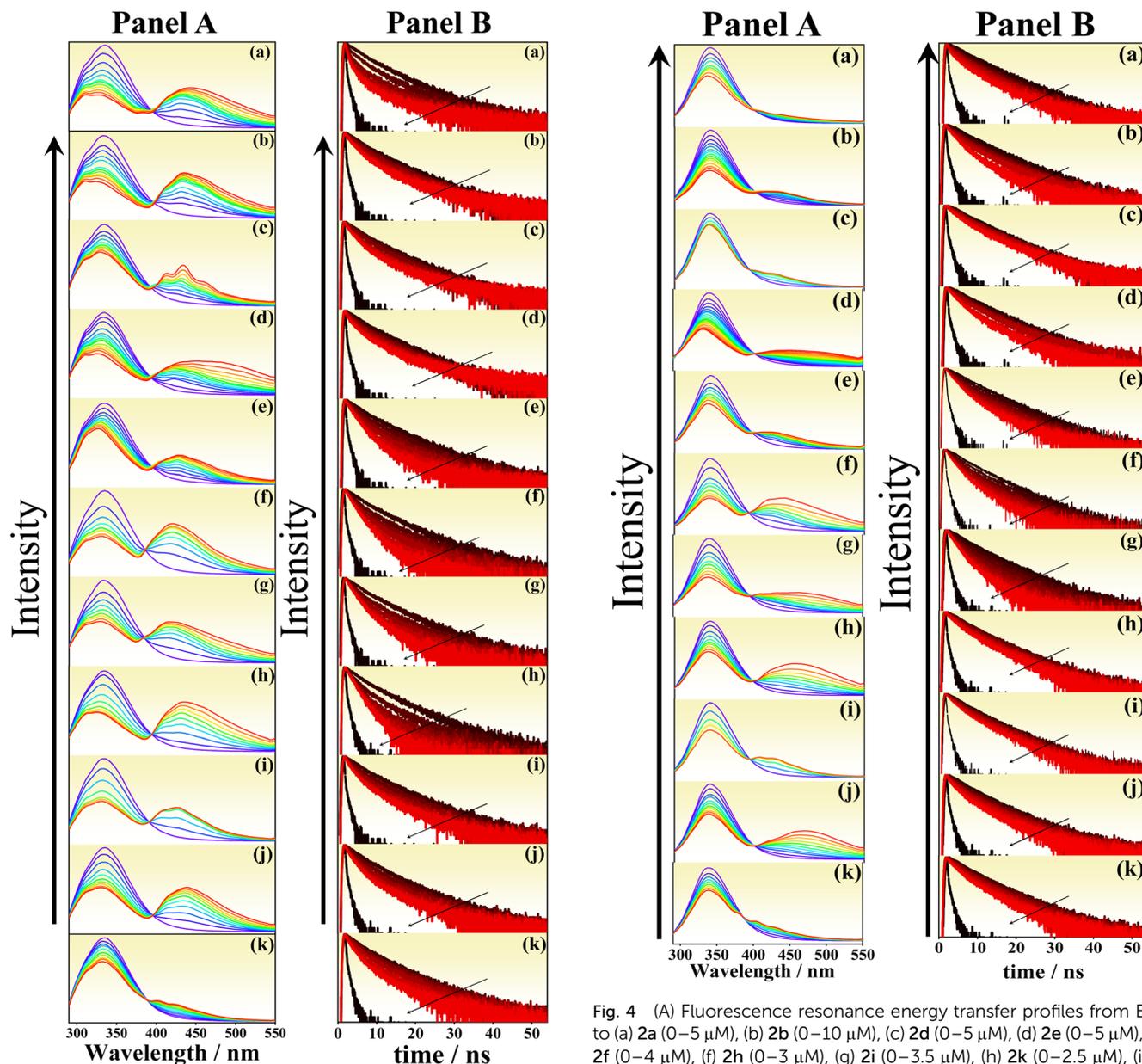**Fig. 3** (A) Fluorescence resonance energy transfer profiles from HSA to (a) **2a** (0−3 μM), (b) **2b** (0−5 μM), (c) **2d** (0−3 μM), (d) **2e** (0−4 μM), (e) **2f** (0−10 μM), (f) **2h** (0−3 μM), (g) **2i** (0−3 μM), (h) **2k** (0−4.5 μM), (i) **2l** (0−2.5 μM), (j) **2m** (0−3 μM) and (k) **2n** (0−2.5 μM) (λ_{ex} = 280 nm). (B) Changes in the fluorescence decay profile of HSA monitored at 325 nm with the consecutive addition of (a) **2a**, (b) **2b**, (c) **2d**, (d) **2e**, (e) **2f**, (f) **2h**, (g) **2i**, (h) **2k**, (i) **2l**, (j) **2m** and (k) **2n** upon excitation at 295 nm. In all the cases, the concentration of HSA was kept at 5 μM.

Fig. 4 (A) Fluorescence resonance energy transfer profiles from BSA to (a) **2a** (0−5 μM), (b) **2b** (0−10 μM), (c) **2d** (0−5 μM), (d) **2e** (0−5 μM), (e) **2f** (0−4 μM), (f) **2h** (0−3 μM), (g) **2i** (0−3.5 μM), (h) **2k** (0−2.5 μM), (i) **2l** (0−2 μM), (j) **2m** (0−3 μM) and (k) **2n** (0−10 μM) (λ_{ex} = 280 nm). (B) Changes in the fluorescence decay profile of BSA monitored at 335 nm with the consecutive addition of (a) **2a**, (b) **2b**, (c) **2d**, (d) **2e**, (e) **2f**, (f) **2h**, (g) **2i**, (h) **2k**, (i) **2l**, (j) **2m** and (k) **2n** upon excitation at 295 nm. In all the cases, the concentration of BSA was kept at 5 μM.

for BSA, only compounds **2i** and **2n** demonstrated superior quenching. Although we cannot directly correlate the higher k_q values to the structural motifs, this phenomenon can be explained in terms of the higher surface hydrophobicity of HSA, which provides the 2*H*-chromene scaffolds with a more favorable hydrophobic environment.[64–66] Despite the presence of two binding sites in BSA, the compounds showed similar k_q values for both proteins, strongly suggesting the site-specific binding of the reported 2*H*-chromenes to BSA.[67]

The dominant mechanism of protein fluorescence diminution is due to the long-range dipole–dipole interaction that is also demonstrated by the higher values of Stern–Volmer constants (K_{SV}) or quenching rate constants (k_q).[68,69] To date, various extrinsic probes have been employed to investigate different subdomains of model proteins such as BSA and HSA. In these studies, the Stern–Volmer quenching constants (K_{SV}) typically fall in the range of 10^4–10^5 L mol^{-1}.[70–75] The synthesized 2*H*-chromenes not only exhibit quenching efficiencies comparable to these classical probes but, in several cases, surpass them. This observation indicates that the fluorescence

Table 3 Different energy transfer and quenching parameters of 2H-chromenes in the presence of HSA and BSA

System	Compound	Energy transfer efficiency (%)	Overlap integral $J(\lambda)$ (M^{-1} cm^{-1} nm^4)	Förster radius (R_0) (Å)	Distance between donor and acceptor (r) (Å)	Stern Volmer constant (K_{SV}) (L mol^{-1})	Rate of energy transfer (k_{ET}) (s^{-1})	Quenching rate constant (k_q) (L mol^{-1} s^{-1})
HSA	2a	0.60	1.293×10^{14}	26.32	24.59	3.24×10^5	2.02×10^8	6.09×10^{13}
	2b	0.55	1.246×10^{14}	26.16	25.29	2.83×10^5	2.30×10^8	5.33×10^{13}
	2d	0.49	1.081×10^{14}	25.54	25.71	2.07×10^5	1.81×10^8	3.91×10^{13}
	2e	0.34	1.732×10^{14}	27.63	30.86	1.11×10^5	9.70×10^7	2.08×10^{13}
	2f	0.31	5.805×10^{15}	23.02	26.31	1.28×10^5	8.46×10^7	2.41×10^{13}
	2h	0.48	2.784×10^{14}	29.91	30.30	5.10×10^5	1.74×10^8	9.55×10^{13}
	2i	0.53	2.911×10^{14}	30.13	29.53	7.33×10^5	2.12×10^8	1.38×10^{13}
	2k	0.47	2.786×10^{14}	29.91	30.51	4.80×10^5	1.67×10^8	9.05×10^{13}
	2l	0.51	1.929×10^{14}	28.13	27.95	6.54×10^5	1.96×10^8	12.32×10^{13}
	2m	0.28	1.706×10^{14}	27.56	32.26	1.51×10^5	7.32×10^7	2.84×10^{13}
	2n	0.51	2.678×10^{14}	29.71	29.41	8.97×10^5	1.97×10^8	11.93×10^{13}
BSA	2a	0.37	1.171×10^{14}	25.86	28.26	0.91×10^5	1.02×10^8	1.58×10^{13}
	2b	0.53	1.697×10^{14}	27.54	26.99	1.76×10^5	1.96×10^8	3.06×10^{13}
	2d	0.48	1.048×10^{14}	25.41	25.75	1.45×10^5	1.61×10^8	2.52×10^{13}
	2e	0.15	1.221×10^{14}	26.07	34.81	1.15×10^5	3.07×10^7	2.01×10^{13}
	2f	0.38	5.676×10^{15}	22.94	24.89	1.84×10^5	1.06×10^8	3.21×10^{13}
	2h	0.52	2.703×10^{14}	29.76	29.36	3.89×10^5	1.89×10^8	6.77×10^{13}
	2i	0.54	2.771×10^{14}	29.88	29.09	6.27×10^5	2.05×10^8	10.93×10^{13}
	2k	0.40	2.774×10^{14}	29.89	31.97	2.63×10^5	1.16×10^8	4.58×10^{13}
	2l	0.41	1.891×10^{14}	28.04	29.79	3.28×10^5	1.21×10^8	5.72×10^{13}
	2m	0.31	1.683×10^{14}	27.49	31.42	0.51×10^5	7.83×10^7	0.89×10^{13}
	2n	0.36	2.594×10^{14}	29.56	32.53	5.56×10^5	9.79×10^7	9.69×10^{13}

of HSA and BSA is quenched through both collisional encounters and complex formation with 2H-chromenes, implying the involvement of mixed dynamic and static quenching mechanisms in the HSA/BSA–2H-chromene system, with the static component being predominant.[70,72] This elevated affinity confirms that the 2H-chromene scaffold forms robust complexes within protein hydrophobic cavities, a prerequisite for efficient FRET applications. Considerable overlap between the fluorescence spectra of proteins and the absorption spectra of the quencher (Fig. S74 and S75) suggests the occurrence of fluorescence resonance energy transfer during the quenching process. The calculated Förster radius (R_0) and the average distances (r) are presented in Table 3. To determine the relative proximity of 2H-chromenes to Trp residues in different proteinous assemblies, we have calculated the energy transfer efficiencies (E) as well (Table 3). The E values for all 2H-chromenes indicate that the chromene moieties can measure the proteinous microenvironment at ~2.6 ± 0.5 nm, close to the Trp of protein; *i.e.*, it can be employed as a nanometric ruler.

To the best of our knowledge, this seems to be the first documentation of extrinsic molecular reporters based on 2H-chromenes that can penetrate deep inside the protein cavity to this extent. In all cases, the r/R_0 ratio lies in the range of 0.8–1.5, which is also an indication of potential FRET pair generation.

2.4. Time-resolved study

Time-resolved studies are considered to be the most sensitive indicator of the local environment in which a given fluorophore is placed and exclusively provide the dynamic information of

the excited state.[76–78] The fluorescence lifetimes of the Trp residues in proteins are a complex function of their interactions with the local environment and the solvent.

There are several possible origins of multi-exponential decay: ground state heterogeneity, time-dependent relaxation around the excited state, or the intrinsic heterogeneity of the Trp residue.[77,78] The time-resolved decay of protein fluorescence (for both HSA and BSA) as a function of 2H-chromene concentration is depicted in Fig. 3 and 4 (Panel B). With the gradual addition of micromolar amounts of the acceptor, a notable diminution of the donor lifetime was observed, and the corresponding decay parameters are stated in Tables S2 and S3. The fluorescence quenching rate constants (k_q) of serum albumins by 2H-chromenes have also been determined utilizing time-resolved fluorescence data from the following relation:

$$\frac{1}{\tau} = \frac{1}{\tau_0} + k_q[Q]$$

where τ and τ_0 are the respective lifetimes of the protein in the presence and absence of the acceptor fluorophores, and [Q] is the concentration of the quencher. Higher values of k_q in the presence of 2H-chromenes indicate the long-range energy transfer process between the chromenes and tryptophan residues on proteins. It is well-known that the energy transfer is dependent on the lifetime of the donor fluorophore (τ_D) and the rate constant of energy transfer ($k_{ET}(r)$), which has been evaluated from the following equation:

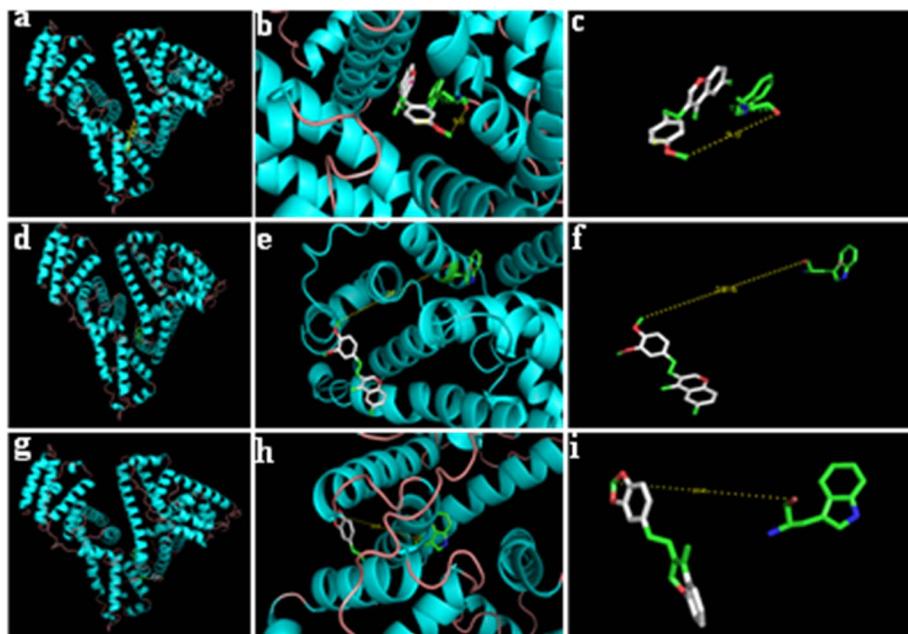$$k_{ET}(r) = \frac{1}{\tau_D}\left(\frac{R_0}{r}\right)^6$$

Fig. 5 Docking results of the chromene–HSA system: the most favorable docked pose of chromenes with HSA (a, d and g); binding sites of chromenes within HSA (b, e and h) (HSA is shown in the ribbon structure, tryptophan and bound chromenes are represented by the stick model); molecular interaction pattern of chromenes in the IIA drug binding site of HSA and magnified stereo views at the site of the interaction of the chromenes with HSA (c, f and i) (the yellow dotted line refers to the distances (in Å) obtained from the docked pose of the Trp 214 residue of HSA from chromenes **2a**, **2b**, and **2d**).

The values of $k_{ET}(r)$ for HSA–chromene and BSA–chromene are detailed in Table 3.

The synthesized 2H-chromene derivatives exhibit Förster critical distances ($R_0 = 27.64 \pm 2.25$ Å for HSA; 27.23 ± 2.09 Å for BSA) that are remarkably equivalent to the canonical tryptophan-ammonium 8-anilino-1-naphthalenesulfonate (ANS) FRET pair ($R_0 = 28.6$ Å),[79] confirming exceptional spectroscopic complementarity for extrinsic protein probing. From the donor–acceptor separations ($r = 24.59$–32.26 Å for HSA & 24.89–34.81 Å for BSA), the mean r/R_0 ratios of 1.03 (HSA) and 1.06 (BSA) position chromenes in the optimal FRET measurement sensitivity window (0.5–2 R_0).[71] The quenching rate constants ($k_q = 6.08 \pm 3.68 \times 10^{13}$ L mol^{-1} s^{-1} for HSA) are many-fold higher than diffusion-controlled dynamic quenching, indicating dominant static quenching through tight complex formation rather than collision-based mechanisms.[65] Critically, lead compounds (**2i**, **2n**, **2l**, and **2a**) simultaneously achieve optimal R_0, minimal r (<27 Å), and superior K_{SV} values ($\sim 10^5$ L mol^{-1}) parameters while maintaining FRET efficiencies ($E = 51$–60%) equivalent to established protein FRET standards. This concurrent optimization across all three parameters, unprecedented for synthetic extrinsic fluorophores, demonstrates that the 2H-chromene scaffold provides a versatile, rationally tunable platform, surpassing conventional probes for HSA-targeted FRET biosensing and protein structural characterization.

2.5. Spectropolarimetric results

Circular dichroism (CD) spectroscopy is a sensitive technique for monitoring the secondary structural changes in proteins. At physiological pH conditions, both HSA and BSA exhibit two negative bands at 209 nm and 222 nm, respectively, in the CD spectra, which confirms the presence of an α-helix in the advanced structure of the protein.[78,80] The consecutive addition of 2H-chromenes did not bring about any considerable changes in the intensity of negative bands of both proteins, which is an indication that the binding of 2H-chromenes did not alter the secondary structure of the protein, especially the R-helix structure. The binding of a fluorophore with serum albumins without hampering the secondary structure is of great significance since their physiological and pharmacological roles (e.g., transportation of several endogenous compounds like fatty acids and bilirubin) remain the same.[21] The effects of differently substituted 2H-chromenes on the secondary structure of HSA and BSA are displayed in Fig. S76 and S77, respectively.

2.6. Molecular docking study

To delineate the efficacy of any bioactive drug molecule as a therapeutic agent, in-depth knowledge regarding its binding sites within the protein is of grave importance. HSA and BSA are both capable of binding with a variety of drugs having similar physicochemical properties, which directly impacts their pharmacokinetics, pharmacodynamics and elimination.[62,78]

HSA has a limited number of binding sites for endogenous and exogenous ligands, which can accommodate different molecules/ligands[49] for transportation through the bloodstream. The binding capacity of HSA varies widely with different ligands. There are seven binding sites present in HSA, labelled as FA1–FA7, which have various binding affinities, contrary to those of hemin or bilirubin, where there is only one primary site

available for drug binding.[80–82] However, recent extensive studies on the crystallographic analysis of drug binding to HSA revealed that binding sites situated in the sub-domains IIA and IIIA are the most primal ones, although additional binding sites across the protein have also been identified.[21,61,83,84] For BSA as well, two principal drug binding sites are present in the hydrophobic cavities of subdomains IIA and IIIA. In general, FRET-based drugs are seen to bind to the hydrophobic IIA region (near Trp 214).[21]

Comprehensive molecular docking and experimental validation revealed that 2H-chromene derivatives consistently demonstrate preferential binding to distinct serum albumin subdomains determined by protein species and scaffold linearity. With HSA, all 2H-chromene minimum energy conformers were positioned within the IIA subdomain (Fig. 5 and S78), with calculated distances from Trp-214 exhibiting excellent agreement with experimentally determined fluorescence spectroscopy measurements (Table S4). This binding localization mirrors the classical warfarin binding site, where the anticoagulant achieves a binding constant of $K_b = 1.06 \times 10^5$ M^{-1},[85] yet 2H-chromenes demonstrate superior binding affinity (K_{SV} $\sim$4.07 $\times$ 10^5 L mol^{-1} for HSA). Critically, no alterations in HSA circular dichroism spectra were observed upon 2H-chromene addition, indicating that these probes penetrate the drug binding pockets through a non-disruptive mechanism, slipping into hydrophobic cavities without inducing secondary structural changes to protein helicity.

Conversely, BSA binding studies revealed species dependent selectivity: molecular docking indicated preferential interaction with Trp-134 (subdomain IB) rather than Trp-213, positioning 2H-chromenes in the IIIA region that is topologically similar to HSA's IIA, but distinct in tryptophan microenvironment

accessibility (Fig. 6 and S79). Notably, ANS interaction with BSA (where binding affinity K_A ranges from 10^2 to 10^4 M^{-1} across multiple pH values) occurs through complex multi-site binding mechanisms involving both electrostatic ion-pairing with cationic amino acid residues (Lys114, Arg185, Arg427) and hydrophobic interactions within Sudlow site II (containing Leu122, Phe133, Lys136, Tyr137, Pro117).[71]

In stark contrast, 2H-chromenes exhibit singular, high-affinity subdomain preferences without evidence of competitive multi-site binding. The almost linear structure of 2H-chromenes, distinct from ANS's bulkier naphthalene-sulfonate geometry, enables preferential access to specific subdomains through spatial orientation optimization. Calculated distances from Trp residues for both HSA and BSA conformations matched experimental fluorescence-derived distances precisely (Table S4), validating the docking predictions and confirming that 2H-chromenes achieve specific geometric positioning within binding pockets. The insertion of 2H-chromenes into IIA (HSA) and IIIA (BSA) binding sites, attributed fundamentally to their linear molecular architecture, contrasts with ANS's behaviour of binding across multiple overlapping sites. This structural distinction provides a mechanistic explanation for the superior binding homogeneity observed with 2H-chromenes, where single, dominant binding sites predominate without the binding site heterogeneity characteristic of ANS-protein systems. The ability of 2H-chromenes to preserve the native secondary structure of HSA, unlike warfarin, which induces conformational changes, or ANS, which promotes multi-site-driven protein flexibility, establishes these compounds as highly selective, orthogonal probes for subdomain-specific protein analysis. By enabling precise protein–ligand characterization without perturbing structural
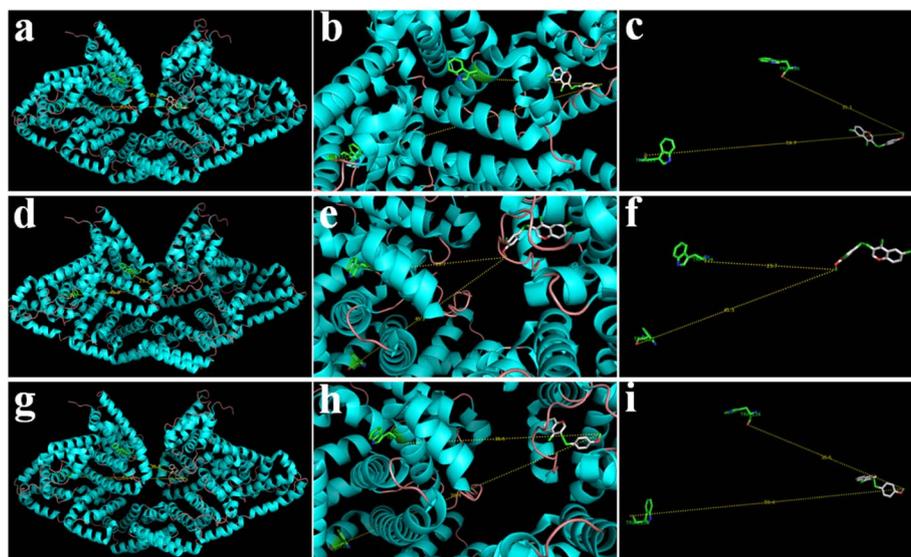

Fig. 6   Docking results of the chromene−BSA system: the most favorable docked pose of chromenes with BSA (a, d and g); binding sites of chromenes within BSA (b, e and h) (BSA is shown in the ribbon structure, tryptophan and bound chromenes are represented by the stick model); molecular interaction pattern of chromenes in the IIIA drug binding site of BSA and magnified stereo views at the site of the interaction of the chromenes with BSA (c, f and i) (the yellow dotted line refers to distances (in Å) obtained from the docked poses of the Trp 134 and Trp 213 residues of BSA from chromenes **2a**, **2b**, and **2d**).

integrity, 2*H*-chromenes emerge as powerful tools for non-invasive investigations of protein interactions.

3. Conclusion

Herein, we have described an operationally simple Grignard addition to variably substituted spiro-4-oxochroman-3,1′-cyclopropanes for the efficient synthesis of a diverse array of *C*-3 functionalized 4-alkyl/allyl/phenyl-3-*E*-styryl-2*H*-chromenes under exceedingly mild conditions with broad functional group tolerance and high yields. Solvent-dependent absorption and fluorescence behavior of a series of prepared chromenes revealed their photophysical signature. Utilizing the steady state and time-resolved fluorescence measurements, the binding phenomena of these 2*H*-chromenes as external energy transfer fluorescent probes with HSA and BSA are systematically monitored, and the results insinuate that 2*H*-chromenes bind with serum albumins with high affinity, resulting in a strong interaction between the system and proteins. The linear-like structure of the chromenes leads to their subtle and effective insertion within the proteins without changing the helicity, which has been further verified by spectropolarimetry. Docking simulation revealed that all the chromenes resided in the vicinity of Trp-214 in the IIA region of HSA and Trp-134 in the IIIA region, rather than Trp-213 in the case of BSA. Keeping in mind the applicability of 2*H*-chromenes in pharmaceutical industries, we earnestly hope that the exploration of these chromene–protein interactions will be of assistance in comprehending the bioavailability of chromene-based drugs and can act as a pertinent model to study diverse biological systems. Further related studies utilizing this novel cyclopropyl ring cleavage reaction for the development of other methodologies are currently underway in our laboratory.

4. Experimental section

4.1. General methods

All commercially available reagents, HSA, BSA, and solvents (Sigma-Aldrich, SRL) were used as received, unless otherwise noted. Solvents were dried and distilled prior to use, following standard procedures. A 0.05 M HEPES buffer (pH 7.4, SRL) was employed for all protein-related studies. Ultrapure water was obtained from a Milli-Q system. ^{1}H and ^{13}C NMR spectra were recorded on a Bruker AVANCE 300 MHz spectrometer (δ in ppm relative to TMS). HRMS data were acquired on an ESI-TOF mass spectrometer (positive mode) in MeCN or MeOH.

4.2. General procedure for the synthesis of *E*-3-arylidene-chroman-4-ones and spiro-4-oxochroman-3,1′-cyclopropanes (1a–1j)

6-Methyl-4-chromanone or 4-chromanone (1.0 equiv.) and aryl aldehydes bearing various substituents (1.0 equiv.) were dissolved in a minimum volume of MeOH and treated with a few drops of concentrated HCl. The reaction mixture was refluxed for 10–12 h to facilitate an acid-catalyzed aldol condensation, and upon cooling to room temperature, the corresponding *E*-3-

arylidene-chroman-4-ones were isolated as crystalline solids by filtration and washing with cold MeOH.

To a solution of the resulting chromanochalcones (2.0 mmol) in CH_2Cl_2 (10 mL), trimethylsulfoxonium iodide (0.572 g, 2.6 mmol), tetrabutylammonium bromide (0.967 g, 3.0 mmol), and 50% aqueous NaOH (0.32 g, 8.0 mmol) were added. The mixture was refluxed for 16–18 h (TLC monitoring) and extracted with Et_2O (3 × 20 mL). The combined organic layers were washed with water (30 mL) and dried over anhydrous Na_2SO_4. Evaporation of the solvent afforded spiro-4-oxochroman-3,1′-cyclopropanes (**1a–1j**) in excellent yields (92–98%), which were used without further purification as substrates for subsequent Grignard additions.

4.3. General procedure for the synthesis of 4-alkyl-3-*E*-styryl-2*H*-chromenes

A 50 mL Schlenk flask was charged with Mg-turnings (0.072 g, 3.0 mmol), 2 crystals of iodine, and anhydrous Et_2O (2 mL). Methyl iodide (0.2 mL, 0.426 g, 3.0 mmol) was added under an inert atmosphere, and the mixture was gently refluxed with stirring for 30 min to form MeMgI. A solution of spiro-4-oxochroman-3,1′-cyclopropanes **1** (1.0 mmol) in anhydrous Et_2O (5 mL) was then added dropwise at 0 °C, and the reaction mixture was refluxed for 4–6 h until completion (as monitored by TLC). The mixture was cooled to room temperature, quenched with saturated aqueous NH_4Cl (10 mL), and stirred for 30 min. The aqueous layer was extracted with Et_2O (3 × 20 mL), washed with water, and dried over anhydrous Na_2SO_4. After evaporation of the solvent, 4-alkyl-3-*E*-styryl-2*H*-chromenes (**2a–2i**) were obtained in good yields.

4.4. General procedure for the synthesis of 4-phenyl-3-*E*-styryl-2*H*-chromenes

Mg turnings (0.072 g, 3.0 mmol), I_2 (2 crystals), and anhydrous Et_2O (2 mL) were combined in a 50 mL Schlenk flask under an inert atmosphere. Iodobenzene (0.4 mL, 0.612 g, 3.0 mmol) was added, and the mixture was refluxed with stirring for 45 min to generate PhMgI. After cooling to 0 °C, a solution of spiro-4-oxochroman-3,1′-cyclopropanes **1** (1 mmol) in anhydrous Et_2O (5 mL) was added dropwise, and the resulting mixture was refluxed for 6 h. Quenching with saturated aqueous NH_4Cl (10 mL), extraction with Et_2O (3 × 20 mL), washing with H_2O, drying over anhydrous Na_2SO_4, and evaporation of the solvent afforded 4-phenyl-3-*E*-styryl-2*H*-chromenes (**2j–2l**).

4.5. General procedure for the synthesis of 4-allyl-3-*E*-styryl-2*H*-chromenes

Allyl bromides are prone to nucleophilic substitution; thus, to suppress side reactions, Mg turnings (0.072 g, 3.0 mmol) were activated with I_2 (2 crystals) in a 50 mL Schlenk flask under an inert atmosphere. A solution of spiro-4-oxochroman-3,1′-cyclopropanes **1** (1.0 mmol) and allyl bromide (0.4 mL, 0.37 g, 3.0 mmol) in anhydrous Et_2O (5 mL) was immediately added at 0 °C. The mixture was refluxed for 6 h (TLC control), cooled to room temperature, and quenched with saturated aqueous NH_4Cl (10 mL) with stirring for 30 min. The aqueous layer was

extracted with Et_2O (3×20 mL), and the combined organic layers were washed with H_2O (20 mL), dried over anhydrous Na_2SO_4, and concentrated to yield 4-allyl-3-E-styryl-2H-chromenes (**2m–2n**) as the final products.

4.6. Spectrophotometric and spectrofluorometric study

UV-vis absorption and steady-state fluorescence spectra were recorded on Shimadzu PharmaSpec 1700 and RF-5301 spectrophotometers, respectively, using 10 mm quartz cuvettes. Fluorescence quantum yields (Φ_f) were determined relative to quinine sulfate as a standard ($\Phi_f = 0.54$ for quinine sulfate in 0.1 N H_2SO_4), using the following equation:

$$\frac{\Phi_s}{\Phi_R} = \frac{A_s}{A_R} \times \frac{(Abs)_R}{(Abs)_s} \times \frac{n_s^2}{n_R^2}$$

where Φ_s and Φ_R are the quantum yields, A_s and A_R are the integrated fluorescence areas, $(Abs)_s$ and $(Abs)_R$ are the absorbance values for the probe and the reference molecule, respectively. n_s and n_R are the corresponding refractive indices of the medium for the probe and the reference molecule.

4.7. Time-resolved study

Time-resolved fluorescence measurements were carried out using a 370 nm nanosecond diode laser (IBH, N-295) with an instrument response time of ~10 ps. Fluorescence decay profiles were recorded and analyzed using the IBH DAS-6 decay analysis software. For all lifetime measurements, the decay curves were analyzed by a single and biexponential iterative fitting program provided by IBH, as expressed by the following:

$$I(t) = \sum_{i-1}^{n} A_i \, e^{\frac{-t}{\tau_i}}$$

where $I(t)$ represents the fluorescence intensity at time t, A_i is the pre-exponential factor for the fraction of the fluorescence intensity, τ_i is the fluorescence lifetime of the emitting species and n is the total number of emitting species. The average fluorescence lifetimes for the triexponential and biexponential decay of fluorescence were calculated from the decay times and pre-exponential factors using the relation shown below:

$$\tau_{avg} = \frac{a_1 \tau_1 + a_2 \tau_2}{a_1 + a_2}$$

4.8. FRET study

To understand the changes in the microenvironment in the vicinity of a chromophore, the fluorescence quenching study was realized in light of the Stern–Volmer equation. The bimolecular quenching rate constant (k_q) and Stern–Volmer quenching constant (K_{SV}) were obtained based on the following equation:[86]

$$\frac{F_0}{F} = 1 + K_{SV}[Q] = 1 + k_q \tau_0 [Q]$$

where F_0 and F denote the respective steady state fluorescence intensities of proteins in the absence and presence of the quencher (2H-chromenes). [Q] is the concentration of the quencher and τ_0 is the average fluorescence lifetime of the protein in the absence of the quencher.

The distance between the chromenes (acceptor) and the albumin proteins (donor) can be evaluated using the Förster mechanism of non-radiative energy transfer, and the following equation is used for this purpose:

$$E = 1 - \frac{F}{F_0} = \frac{R_0^6}{R_0^6 + r^6}$$

where E denotes the efficiency of energy transfer between the donor and the acceptor, R_0 is the Förster radius (the critical distance when the energy transfer efficiency is 50%), and r is the distance between the donor and the acceptor. F_0 and F denote the steady state fluorescence intensities of proteins in the presence and absence of the quencher, respectively.

R_0 can be measured by the given equation:

$$R_0^6 = 8.79 \times 10^{-25} \times \chi^2 \times n^{-4} \times \Phi \times J$$

χ^2 is the orientation factor related to the geometry of the donor and the acceptor; usually, it is assumed to be 2/3, which is the value for the donors and the acceptors that randomize by rotational diffusion prior to energy transfer. n is the average refractive index of the medium within the wavelength range where spectral overlap is significant. Φ is the fluorescence quantum yield of the proteins. J is the spectral overlap integral between the emission spectrum of the donor and the absorption spectrum of the acceptor. The spectral overlap integral (J) between the donor emission spectrum and the acceptor absorbance spectrum was approximated by the following summation:

$$J = \frac{\int_0^\infty F(\lambda)\varepsilon(\lambda)\lambda^4 d\lambda}{\int_0^\infty F(\lambda)d\lambda}$$

where $F(\lambda)$ is the corrected fluorescence intensity of the donor in the wavelength range from λ to $\lambda + \Delta\lambda$; $\varepsilon(\lambda)$ is the extinction coefficient of the acceptor at λ.

4.9. Spectropolarimetric studies

Circular dichroism (CD) spectra were recorded on a Jasco J-815 spectropolarimeter (Jasco International Co., Japan) equipped with a PFD-425L/15 thermal programmer and temperature controller interfaced in a rectangular quartz cuvette of 1 cm path length. Spectra were collected over 195–300 nm with a scan speed of 100 nm min^{-1} and a bandwidth of 10 nm at 298 K. Each spectrum was obtained by averaging five scans, smoothed to improve the signal-to-noise ratio, and corrected for baseline contributions.

4.10. Molecular docking

AutodockVina 1.1.0-based molecular docking[87] was utilized to investigate chromene binding sites on HSA (PDB ID: 1AO6) and BSA (PDB ID: 4F5S), obtained from the Protein Data Bank (https://www.rcsb.org/pdb). Ligand and receptor structures were prepared with MGLTools 1.5.4, and chromene geometries were optimized by DFT calculations (B3LYP/6-31G(d,p)) using Gaussian 09 (ref. 88) prior to conversion to

Vina-compatible formats. Docking employed default Vina parameters with a grid box encompassing the putative binding site; the lowest-energy conformation was selected as the preferred binding pose. Results were visualized and analyzed in PyMOL,[89] including measurements of interatomic distances between chromenes and protein residues.

Conflicts of interest

The authors declare no conflict of interest.

Data availability

The data supporting this article have been included as part of the supplementary information (SI). Supplementary information: [1H], [13C] NMR, and HRMS spectra, photophysical data, details of time resolved data, CD spectra, and docking results. See DOI: https://doi.org/10.1039/d5ra07616a.

References

1 M. Costa, T. A. Dias, A. Brito and F. Proença, *Eur. J. Med. Chem.*, 2016, **123**, 487–507.
2 E. A. Couladouros and A. T. Strongilos, *Angew. Chem., Int. Ed.*, 2002, **41**, 3677–3680.
3 S.-L. Zheng and L. Chen, *Org. Biomol. Chem.*, 2021, **19**, 10530–10548.
4 L. Zhang and Z. Xu, *Eur. J. Med. Chem.*, 2019, **181**, 111587.
5 B. Sandhya, D. Giles, V. Mathew, G. Basavarajaswamy and R. Abraham, *Eur. J. Med. Chem.*, 2011, **46**, 4696–4701.
6 X. H. Zhang, B. J. Chen, X. Q. Lin, O. Y. Wong, C. S. Lee, H. L. Kwong, S. T. Lee and S. K. Wu, *Chem. Mater.*, 2001, **13**, 1565–1569.
7 C. M. Sousa, J. Pina, J. Seixas De Melo, J. Berthet, S. Delbaere and P. J. Coelho, *Eur. J. Org. Chem.*, 2012, **9**, 1768–1773.
8 R. Roy, S. Rakshit, T. Bhowmik, S. Khan, A. Ghatak and S. Bhar, *J. Org. Chem.*, 2014, **79**, 6603–6614.
9 N. Majumdar, N. D. Paul, S. Mandal, B. De Bruin and W. D. Wulff, *ACS Catal.*, 2015, **5**, 2329–2366.
10 G. Savitha, K. Felix and P. T. Perumal, *Synlett*, 2009, **13**, 2079–2082.
11 A. Carral-Menoyo, A. Misol, M. Gómez-Redondo, N. Sotomayor and E. Lete, *J. Org. Chem.*, 2019, **84**, 2048–2060.
12 Z. Zhou, M. Bian, L. Zhao, H. Gao, J. Huang, X. Liu, X. Yu, X. Li and W. Yi, *Org. Lett.*, 2018, **20**, 3892–3896.
13 E. Calcio Gaudino, S. Tagliapietra, K. Martina, G. Palmisano and G. Cravotto, *RSC Adv.*, 2016, **6**, 46394–46405.

14 L. Mahendar and G. Satyanarayana, *J. Org. Chem.*, 2014, **79**, 2059–2074.
15 X. Xu, J. Hu, H. Xue, Y. Hu, Y. Liu, G. Lin, L. Liu and R. Xu, *Int. J. Biol. Macromol.*, 2023, **253**, 126914.
16 S. Ashraf, H. Qaiser, S. Tariq, A. Khalid, H. A. Makeen, H. A. Alhazmi and Z. Ul-Haq, *Curr. Res. Struct. Biol.*, 2023, **6**, 100114.
17 A. J. Sawyer and T. R. Kyriakides, *Adv. Drug Delivery Rev.*, 2016, **97**, 56–68.
18 U. Bickel, T. Yoshikawa and W. M. Pardridge, *Adv. Drug Delivery Rev.*, 2001, **46**, 247–279.
19 E. Ezan, *Adv. Drug Delivery Rev.*, 2013, **65**, 1065–1073.
20 N. Goswami, A. Makhal and S. K. Pal, *J. Phys. Chem. B*, 2010, **114**, 15236–15243.
21 S. Datta and M. Halder, *J. Phys. Chem. B*, 2014, **118**, 6071–6085.
22 J. I. Lee, L. Zhang, A. Y. Men, L. A. Kenna and S. M. Huang, *Clin. Pharmacokinet.*, 2010, **49**, 295–310.
23 I. Vayá, V. Lhiaubet-Vallet, M. C. Jiménez and M. A. Miranda, *Chem. Soc. Rev.*, 2014, **43**, 4102–4122.
24 T. Werner, M. B. Morris, S. Dastmalchi and W. B. Church, *Adv. Drug Delivery Rev.*, 2012, **64**, 323–343.
25 D. Shukla, C. P. Schneider and B. L. Trout, *Adv. Drug Delivery Rev.*, 2011, **63**, 1074–1085.
26 K. Wanat, *Mol. Biol. Rep.*, 2020, **47**, 3221–3231.
27 X. Yan, Z. Li, H. Liu, Z. Wang, J. Fan, C. Xie, Q. Li and J. Xu, *J. Photochem. Photobiol., A*, 2022, **422**, 113576.
28 G. L. Trainor, *Expert Opin. Drug Discovery*, 2007, **2**, 51–64.
29 D. C. Carter, X. He, S. H. Munson, P. D. Twigg, K. I. M. M. Gernert, M. B. Broom and T. Y. Miller, *Science*, 1989, **244**, 1195–1198.
30 B. X. Huang and H. Kim, *J. Am. Soc. Mass Spectrom.*, 2004, **15**, 1237–1247.
31 D. K. Sahoo, S. Dasgupta, T. Kistwal and A. Datta, *Int. J. Biol. Macromol.*, 2023, **226**, 1515–1522.
32 R. E. Lyle and L. P. Paradis, *J. Am. Chem. Soc.*, 1955, **77**, 6667–6668.
33 D. Basavaiah and M. Bakthadoss, *Chem. Commun.*, 1998, 1639–1640.
34 A. Merz and G. Märkl, *Angew. Chem., Int. Ed. Engl.*, 1973, **12**, 845–846.
35 E. C. Ashby, J. Laemmle and H. M. Neumann, *J. Am. Chem. Soc.*, 1972, **94**, 5421–5434.
36 D. K. Rana, S. Rakshit, S. Dhar and S. C. Bhattacharya, *J. Photochem. Photobiol., A*, 2013, **270**, 67–74.
37 S. S. Mati, S. Chall, S. Rakshit and S. C. Bhattacharya, *J. Fluoresc.*, 2015, **25**, 341–353.
38 M. Kaya and E. Menteşe, *J. Heterocycl. Chem.*, 2020, **57**, 1714–1719.
39 V. Joseph, K. R. J. Thomas, M. Singh, S. Sahoo and J. H. Jou, *Eur. J. Org. Chem.*, 2017, **2017**, 6660–6670.
40 D. Patra and C. Barakat, *Spectrochim. Acta, Part A*, 2011, **79**, 1034–1041.
41 D. Panda and A. Datta, *J. Chem. Phys.*, 2006, **125**, 054513.
42 A. Al-Kawkabani, M. Makhloufi-Chebli, N. Benosmane, B. Boutemeur-Kheddis, M. Hamdi and A. M. S. Silva, *J. Mol. Struct.*, 2017, **1146**, 285–291.

43 M. Makhloufi-Chebli, S. M. Hamdi, A. Rabahi, A. M. S. Silva and M. Hamdi, *J. Mol. Liq.*, 2013, **181**, 89–96.

44 S. Jana, S. Dalapati, S. Ghosh, S. Kar and N. Guchhait, *J. Mol. Struct.*, 2011, **998**, 136–143.

45 Y. Gong, X. Guo, S. Wang, H. Su, A. Xia, Q. He and F. Bai, *J. Phys. Chem. A*, 2007, **111**, 5806–5812.

46 A. Kawski and P. Bojarski, *Spectrochim. Acta, Part A*, 2011, **82**, 527–528.

47 A. Bhattacharyya, S. Ghosh, S. C. Makhal and N. Guchhait, *Spectrochim. Acta, Part A*, 2017, **183**, 306–311.

48 A. Mallick, B. Haldar and N. Chattopadhyay, *J. Phys. Chem. B*, 2005, **109**, 14683–14690.

49 P. Banerjee, S. Pramanik, A. Sarkar and S. C. Bhattacharya, *J. Phys. Chem. B*, 2009, **113**, 11429–11436.

50 L. Stryer, *Annu. Rev. Biochem.*, 1978, **47**, 819–846.

51 C. G. Dos Remedios and P. D. J. Moens, *J. Struct. Biol.*, 1995, **115**, 175–185.

52 K. Truong and M. Ikura, *Curr. Opin. Struct. Biol.*, 2001, **11**, 573–578.

53 A. Kawski, *Ann. Phys.*, 1948, **2**, 55–75.

54 C. X. Yin, K. M. Xiong, F. J. Huo, J. C. Salamanca and R. M. Strongin, *Angew. Chem., Int. Ed.*, 2017, **56**, 13188–13198.

55 S. Henrich, O. M. H. Salo-Ahen, B. Huang, F. Rippmann, G. Cruciani and R. C. Wade, *J. Mol. Recognit.*, 2010, **23**, 209–219.

56 J. Das, *Chem. Rev.*, 2011, **111**, 4405–4417.

57 S. Jana, S. Ghosh, S. Dalapati and N. Guchhait, *Photochem. Photobiol. Sci.*, 2012, **11**, 323–332.

58 J. M. Goldberg, L. C. Speight, M. W. Fegley and E. J. Petersson, *J. Am. Chem. Soc.*, 2012, **134**, 6088–6091.

59 X. Qin, X. Yang, L. Du and M. Li, *RSC Med. Chem.*, 2021, **12**, 1826–1838.

60 S. Patel and A. Datta, *J. Phys. Chem. B*, 2007, **111**, 10557–10562.

61 S. Patel, K. K. Sharma and A. Datta, *Spectrochim. Acta, Part A*, 2015, **138**, 925–931.

62 S. Dhar, D. K. Rana, A. Pal and S. C. Bhattacharya, *J. Photochem. Photobiol., B*, 2013, **129**, 69–77.

63 X. Pang and H.-X. Zhou, *Annu. Rev. Biophys.*, 2017, **46**, 105–130.

64 R. Maier, M. R. Fries, C. Buchholz, F. Zhang and F. Schreiber, *Cryst. Growth Des.*, 2021, **21**, 5451–5459.

65 V. Nho Tran, J. E. M. Rivas, S. Hussain, W. C. Tseng, A. Akentiev, B. Noskov, G. Loglio and S. Y. Lin, *J. Mol. Liq.*, 2023, **391**, 123285.

66 Y. Akdogan, J. Reichenwallner and D. Hinderberger, *PLoS One*, 2012, **7**, e45681.

67 X. Han, F. Tian, Y. Ge, F. Jiang, L. Lai, D. Li, Q. Yu, J. Wang, C. Lin and Y. Liu, *J. Photochem. Photobiol., B*, 2012, **109**, 1–11.

68 B. K. Paul, A. Samanta and N. Guchhait, *J. Phys. Chem. B*, 2010, **114**, 6183–6196.

69 B. K. Paul, D. Ray and N. Guchhait, *Phys. Chem. Chem. Phys.*, 2013, **15**, 1275–1287.

70 X. Ma, Z. Shen, X. Liang, J. Wang, H. Wang, M. Wang and X. Yu, *Bioorg. Chem.*, 2025, **165**, 108988.

71 A. Jain, E. Judy and N. Kishore, *J. Phys. Chem. B*, 2024, **128**, 5344–5362.

72 J. Zhang, X. Gao, J. Huang and H. Wang, *ACS Omega*, 2020, **5**, 16833–16840.

73 Y. Wang, J. Li, X. Li, B. Gao, J. Chen and Y. Song, *Sci. Rep.*, 2025, **15**, 8055.

74 M. Garg, E. T. Tamboli, M. Singh, K. Chester, M. Z. Abdin, R. Chandna and S. Ahmad, *Indian J. Pharm. Educ. Res.*, 2015, **49**, 231–239.

75 C. Ràfols, S. Amézqueta, E. Fuguet and E. Bosch, *J. Pharm. Biomed. Anal.*, 2018, **150**, 452–459.

76 D. Singharoy, S. S. Mati, S. Rakshit, S. Chall and S. C. Bhattacharya, *J. Mol. Liq.*, 2016, **213**, 33–40.

77 B. K. Paul and N. Guchhait, *J. Phys. Chem. B*, 2011, **115**, 10322–10334.

78 D. Ray, A. Kundu, A. Pramanik and N. Guchhait, *J. Phys. Chem. B*, 2015, **119**, 2168–2179.

79 D. Matulis, C. G. Baumann, V. A. Bloomfield and R. E. Lovrien, *Biopolymers*, 1999, **49**, 451–458.

80 O. K. Abou-Zied, N. Al-Lawatia, M. Elstner and T. B. Steinbrecher, *J. Phys. Chem. B*, 2013, **117**, 1062–1074.

81 G. Rabbani, M. H. Baig, E. J. Lee, W. K. Cho, J. Y. Ma and I. Choi, *Mol. Pharm.*, 2017, **14**, 1656–1665.

82 S. Rakshit, A. Sarkar and S. C. Bhattacharya, *Colloids Surf., B*, 2017, **155**, 390–398.

83 D. P. Yeggoni, M. Gokara, D. Mark Manidhar, A. Rachamallu, S. Nakka, C. S. Reddy and R. Subramanyam, *Mol. Pharm.*, 2014, **11**, 1117–1131.

84 M. Calvaresi and F. Zerbetto, *J. Chem. Inf. Model.*, 2011, **51**, 1882–1896.

85 H. Rimac, C. Dufour, Ž. Debeljak, B. Zorc and M. Bojić, *Molecules*, 2017, **22**, 1153.

86 S. Rakshit, S. Das, P. Poonia, R. Maini, A. Kumar and A. Datta, *J. Phys. Chem. B*, 2020, **124**, 7484–7493.

87 A. Allouche, *J. Comput. Chem.*, 2012, **32**, 174–182.

88 M. J. Frisch, G. W. Trucks, H. B. Schlegel, G. E. Scuseria, M. A. Robb, J. R. Cheeseman, G. Scalmani, V. Barone, G. A. Petersson, H. Nakatsuji, X. Li, M. Caricato, A. Marenich, J. Bloino, B. G. Janesko, R. Gomperts, B. Mennucci, H. P. Hratchian, J. V. Ortiz, A. F. Izmaylov, J. L. Sonnenberg, D. Williams-Young, F. Ding, F. Lipparini, F. Egidi, J. Goings, B. Peng, A. Petrone, T. Henderson, D. Ranasinghe, V. G. Zakrzewski, J. Gao, N. Rega, G. Zheng, W. Liang, M. Hada, M. Ehara, K. Toyota, R. Fukuda, J. Hasegawa, M. Ishida, T. Nakajima, Y. Honda, O. Kitao, H. Nakai, T. Vreven, K. Throssell, J. A. Montgomery Jr, J. E. Peralta, F. Ogliaro, M. Bearpark, J. J. Heyd, E. Brothers, K. N. Kudin, V. N. Staroverov, T. Keith, R. Kobayashi, J. Normand, K. Raghavachari, A. Rendell, J. C. Burant, S. S. Iyengar, J. Tomasi, M. Cossi, J. M. Millam, M. Klene, C. Adamo, R. Cammi, J. W. Ochterski, R. L. Martin, K. Morokuma, O. Farkas, J. B. Foresman, and D. J. Fox, *Gaussian 09, Revision A.02*, Gaussian, Inc., Wallingford CT, 2016.

89 L. Schrödinger and W. DeLano, *PyMOL*, 2020, available at http://www.pymol.org/pymol.